Supporting Information

18.73% Efficient and Stable Inverted Organic Photovoltaics Featuring a Hybrid Hole-Extraction Layer

Yuanbao Lin[a,b]*, Yadong Zhang[c], Artiom Magomedov[d], Eleftheria Gkogkosi[e], Junxiang Zhang[c], Xiaopeng Zheng[a], Abdulrahman El-Labban[a], Stephen Barlow[c], Vytautas Getautis[d], Ergang Wang[h], Leonidas Tsetseris[e], Seth R Marder[d], Iain McCulloch[b], Thomas D. Anthopoulos[a]*

Experimental details

Solar Cell Fabrication: PFN-Br, PM6, and BTP-eC9 were purchased from Solarmer Materials Inc. PM7-Si was synthesised following previously reported procedures.[1] Br-2PACz was also synthesised as previously described.[2] The ZnO precursor solution was prepared by dissolving 200 mg of zinc acetate dihydrate in 2 mL of 2-methoxyethanol and 60 µl of 2-aminoethanol. Indium tin oxide (ITO) coated glass substrates (Kintec Company, 10 Ω sq.$^{-1}$) were cleaned by sequential ultrasonication in dilute Extran 300 detergent solution, deionised water, acetone, and isopropyl alcohol for 10 min each. The substrates were then subjected to a UV-ozone treatment step for 20 min. Next, ZnO precursor solution was spin-coated onto the substrates and then dried on a hot plate at 200 °C for 0.5 h. The samples were then transferred into a dry nitrogen glove box (≈ 10 ppm O_2). After cooling down, the PFN-Br solution (0.5 mg/ml in methanol) was spin-coated on the ZnO film. PM6:PM7-Si:BTP-eC9 (ratio 0.9:0.1:1.2, 17.5 mg mL^{-1} in chloroform and added 0.5 vol% DIO) were then spun at 3500 rpm for 30 s to obtain an active-layer thickness around 110 nm. After spin-coating, the substrates were annealed at 100 °C for 10 min. After cooling down, the Br-2PACz solution (0.9 mg mL^{-1} in ethanol) was spun at 3000 rpm for 30 s. We note that some white particles appear on the surface of the BHJ/Br-2PACz layer when the SAM solution is deposited onto warm BHJ layers (i.e. above room temperature) and is allowed to wet (i.e. rest on it) its surface for a relatively long period (over 10 s) before spinning. To avoid this, the BHJ layers were allowed to cool to room temperature after the annealing step followed by the immediate spin-coating of the Br-2PACz solution directly onto the BHJ without any wetting period (i.e. immediate after application). Moreover, because the Br-2PACz layer is not strongly attached on BHJ tightly, so any washing process i.e. spin-coating ethanol solvent, will remove the Br-2PACz on BHJ. Finally, the samples were placed in a thermal evaporator and 7 nm of MoO_3 and 100 nm of silver were then thermally evaporated at 5×10^{-7} mbar through a 0.1 cm^2 pixel area shadow mask.

Device Characterisation: UV-vis. spectra were recorded on a Cary 5000 instrument in single beam mode. *J-V* measurements of solar cells were performed in an N_2 filled glove box using a Keithley 2400 source meter and an Oriel Sol3A Class AAA solar simulator calibrated to 1 sun, AM1.5G, with a KG-5 silicon reference cell certified by Newport. The shadow mask with an aperture area of 0.0784 cm^2 was used for *J-V* measurement. The EQE spectra were measured through the Solar Cell Spectral Response Measurement System QE-R3011 (Enli Technology Co., Ltd., Taiwan). For Bruker atomic force microscope (AFM) was used to image the surface of the various layers in tapping mode. Scanning electron microscopy (SEM) measurements were performed using a Zeiss Auriga microscope equipped with in-lens detector. TOF-SIMS measurement (Hiden Analytical Company (Warrington-UK)) operated under vacuum conditions (10^{-9} torr), typically. A continuous Ar^+ beam was employed at 4 keV to sputter the surface while the selected ions were sequentially collected using a MAXIM spectrometer equipped with a quadrupole analyser. The raster of the sputtered area is estimated to be $750 \times 750\ \mu m^2$. The acquisition area from which the depth profiling data are obtained was $\approx 75 \times 75\ \mu m^2$. The charge carrier mobilities of the devices investigated were determined by fitting the measured dark current-voltage curves using the space-charge-limited current (SCLC) model. The hole-only device structure fabricated and used for this study consisted of glass/ITO/PEDOT:PSS/BHJ/Br-2PACz/MoO_3/Ag. The electric-field dependent SCLC mobility was estimated using Equation S1:

$$J\,(V) = \frac{9}{8}\varepsilon_0\varepsilon_r\mu_0 exp\left(0.89\beta\sqrt{\frac{V - V_{bi}}{L}}\right)\frac{(V - V_{bi})^2}{L^3} \qquad \text{(Eq. S1)}$$

Term definition	Symbol	Units
zero-field mobility	μ_0	$cm^2\ V^{-1}\ s^{-1}$
film thickness	L	cm
dark current density	J	$mA\ cm^{-2}$
voltage	V	V
vacuum permittivity	ε_0 (88.54×10^{-12})	$mA\ s\ V^{-1}\ cm^{-1}$
dielectric constant	ε_r (3)	
field activation factor	β	$cm^{1/2}\ V^{-1/2}$

Stability Test: For the annealing test, the samples were stored in the nitrogen gas-filled glovebox by continuous aging at 80 °C on hotplate, and the devices were only exposed to light during the *J-V* measurements. For the illuminated test, the samples were stored in the nitrogen gas-filled glovebox by continuous exposure to white LED light (at 100 mW cm^{-2}).

Light-Intensity Dependence Measurements: Light-intensity dependence measurements were performed with PAIOS instrumentation (Fluxim) (steady-state and transient modes). Transient photo-voltage (TPV) measurements monitor the photovoltage decay upon a small optical perturbation during various constant light-intensity biases and at open-circuit bias conditions. Variable light-intensity bias lead to a range of measured V_{OC} values that were used for the analysis. During the measurements a small optical perturbation (<3% of the V_{OC}, so that $\Delta V_{OC} << V_{OC}$) was applied. The subsequent voltage decay was then recorded to directly monitor bimolecular charge carrier recombination. The photovoltage decay kinetics of all devices follow a mono-exponential decay: $\delta V = A \exp(-t/\tau)$, where t is the time and τ is the charge carrier lifetime. Photo-CELIV measurements (ramp rate 200 V ms^{-1}, delay time: 0 s, offset voltage: 0 V, light-pulse length: 100 μs) were also performed using PAIOS for different light intensities. The light intensity is given in the maximum power of the LED source (100% ≈ 200 mW cm^{-2}).

Electrochemical Impedance Spectroscopy (EIS): EIS was conducted using a commercially available PAIOS. The measurements were performed under open circuit voltage conditions for the OPV in the dark, and in the frequency range between 300 Hz to 3 MHz.

UPS measurement: UPS was performed with a vacuum ultraviolet (VUV) He (1) discharge line 21.22 eV (focus) and a Sphera II EAC 125 7-channeltron electron analyser. A small component ca. 2% β (23.09 eV) was present. The sample was positioned at 0° with respect to the analyser-to-sample plane. Fermi level calibration was performed using an Ar^+ sputtered clean metallic Ag foil in electrical contact to the manipulator holding the sample in contact with the electron analyser. During UPS, a bias of -9.97 eV was applied to observe the secondary electron cutoff. Subsequent measurements were made in electrical contact with thin films to prevent surface charging. UPS Scans were measured from low to high kinetic energy at a constant analyser pass energy of 10 eV and subsequent scans were carefully monitored to detect beam-induced degradation or evidence of charging.

Density Functional Theory calculations: The results were obtained with the Density Functional Theory (DFT) code Vienna Ab Initio Simulation Package (VASP)[3] with a plane-wave basis (and an energy cutoff of 500 eV), projector augmented waves (PAW) [4] and the generalised gradient approximation (GGA) Perdew-Burke-Ernzerhof[5] exchange-correlation (xc) functional. To simulate the effect of molecular adsorption on MoO_3 we used slabs with 3 MoO_3 layers in a 2x2 supercell geometry (with a total of 96 atoms in the pristine, i.e. adsorbate-free, case). Structures were rendered with the software VESTA[6]. Averaging of the electrostatic potential was performed with VASPKIT.[7]

Table S1. A summary of reported PCE values for inverted and standard OPVs utilising different HTLs.

Type	HTL	Structure	BHJ	PCE (%)	Ref.
Inverted	MoO_3	ITO/ZnO/PFN-Br/BHJ/Br-2PACz/MoO_3/Ag	PM6:PM7-Si:BTP-eC9	18.7	This work
	MoO_3	ITO/ZnO/BHJ/MoO_3/Ag	PM6:L8-BO	18.1	8
	MoO_3	Ag/ZnO-NP/SAM/BHJ/MoO3/Ag/TeO2	PM6:Y6	17.5	9
	MoO_3	ITO/ZnO/PEIE/BHJ/MoO_3/Ag	PM6:Y6-HU	17.4	10
	MoO_3	ITO/ZnO:Zr/BHJ/MoO_3/Ag	PM6:Y6:$PC_{71}BM$	17.2	11
	MoO_3	ITO/ZnO/BHJ/MoO_3/Ag	PM6:Y6: $PC_{71}BM$	17.1	12
	MoO_3	ITO/ZnO/BHJ/MoO_3/Ag	PM6:Y18	16.5	13
	MoO_3	ITO/ZnO/BHJ/MoO_3/Ag	PM6:BTP-4Cl	16.5	14
	MoO_3	ITO/ZnO/BHJ/MoO_3/Ag	PTQ11:TPT10	16.3	15
	MoO_3	ITO/ZnO/BHJ/MoO_3/Ag	PM6:BTIC-2Br-m	16.1	16
	PEDOT:F	ITO/PEI-Zn/BHJ/PEDOT:F/Ag	PM6:BTP-eC9:$PC_{71}BM$	17.0	17
	PIDT-F:PMA	ITO/ZnO/BHJ/PIDT-F:PMA/Ag	PM6:BTP-eC9	16.9	18
Standard	PEDOT:PSS	ITO/PEDOT:PSS/BHJ/PNDIT-F3N/Ag	PM6:D18:L8-BO	19.6	19
	PEDOT:PSS	ITO/PEDOT:PSS/BHJ/PNDIT-F3N/Ag	PM1:L8-BO:BTP-2F2Cl	19.2	20
	PEDOT:PSS	ITO/PEDOT:PSS/BHJ/PDIN/Ag	D18:L8-BO	19.1	21
	PEDOT:PSS	ITO/PEDOT:PSS/BHJ/PNDIT-F3N/Ag	PTQ-10:BTP-FTh:IDIC	19.1	22
	PEDOT:PSS	ITO/PEDOT:PSS/BHJ/PNDIT-F3N-Br/Ag	D18/BS3TSe-4F:Y6-O	19.0	23
	PEDOT:PSS	ITO/PEDOT:PSS/BHJ/PNDIT-F3N-Br/Ag	PM6:HDO-4Cl:eC9	18.9	24
	PEDOT:PSS	ITO/PEDOT:PSS/BHJ/PFN-Br/Ag	PM6:BTP-eC9:BTP-S9	18.8	25
	PEDOT:PSS	ITO/PEDOT:PSS/BHJ/PNDIT-F3N/Ag	PM6:BTP-eC9:L8-BO-F	18.7	26
	PEDOT:PSS	ITO/PEDOT:PSS/BHJ/PNDIT-F3N-Br/Ag	PM6:PB2F:BTP-eC9	18.6	27
	Br-2PACz	ITO/Br-2PACz/BHJ/PFN-Br/Ag	PM6:BTP-eC9:$PC_{71}BM$	18.4	28
	PEDOT:PSS	ITO/PEDOT:PSS/BHJ/PNDIT-F3N-Br/Ag	PM6:L8-BO	18.3	10
	Br-2PACz	ITO/Br-2PACz/BHJ/PNDIT-F3N/Ag	PM6:PM6-Si30:BTP-S9	18.3	29

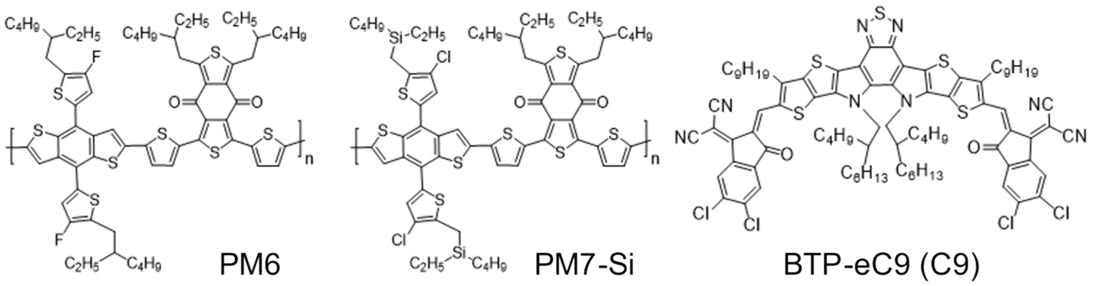

Fig. S1. Chemical structures of donor and acceptor used in this study.

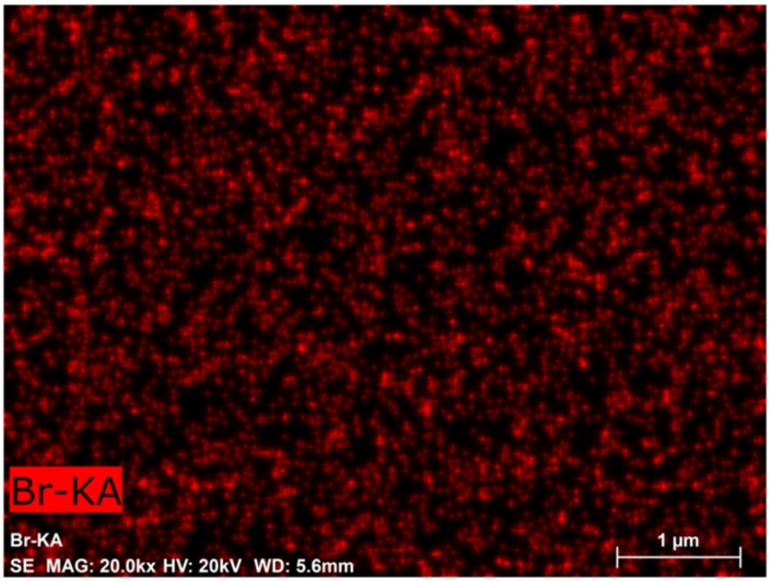

Fig. S2. SEM-EDX mapping for a BHJ/Br-2PACz film.

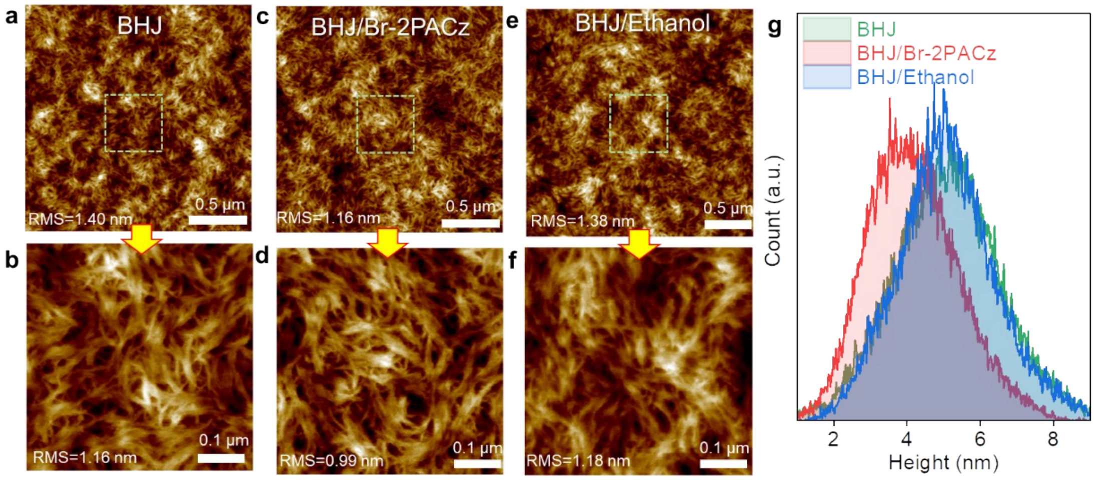

Fig. S3. AFM topography images of BHJ (a)-(b) without, (c)-(d) with Br-2PACz, (e)-(f) spin-coated with pure ethanol, while (b), (d) ,and (f) are the high-resolution AFM corresponding to the green frame in the (a)-(c). (e) Surface height histograms extracted from the AFM images in (b), (d), and (f).

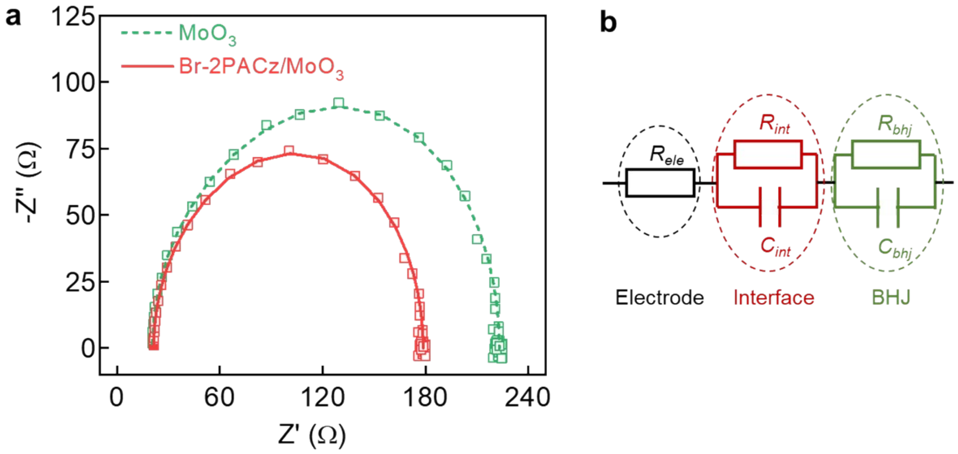

Fig. S4. (a) EIS of OPV cells with MoO_3 and Br-2PACz/MoO_3 HTLs. (a) The equivalent-circuit model is employed for EIS fitting of the devices. R_{ele} corresponds to electrode resistance including ITO and Ag; R_{int} and C_{int} parallel connection corresponds to resistance and capacitance of the interface layer; R_{bhj} and C_{bhj} parallel connection corresponds to resistance and capacitance of the BHJ layer.

Table S2. Fitting parameters to the Nyquist plots for OPVs utilising MoO_3 and Br-2PACz/MoO_3 as the HTLs. R_{ele} corresponds to electrode resistance including ITO and Ag; R_{int} and C_{int} parallel connection corresponds to resistance and capacitance of the interface layer; R_{bhj} and C_{bhj} parallel connection corresponds to resistance and capacitance of the BHJ layer.

HEL	R_{ele} [Ω]	R_{inter} [Ω]	C_{inter} [nF]	R_{bhj} [Ω]	C_{bhj} [nF]
MoO_3	20.5	50.3	18.7	152.5	21.8
Br-2PACz/MoO_3	21.3	36.7	35.3	120.8	28.5

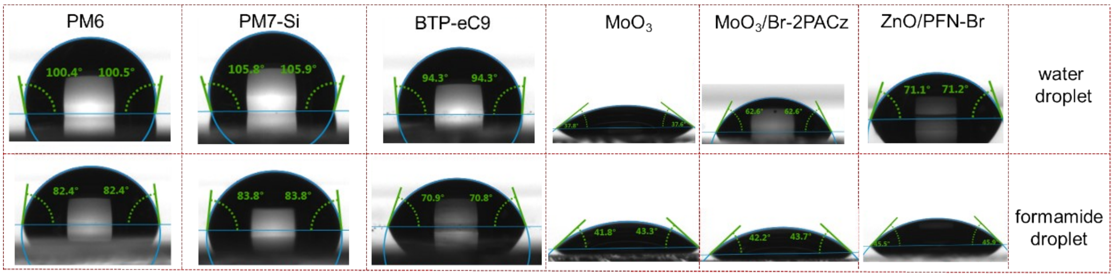

Fig. S5. Photographs of water (top row) and formamide (bottom row) droplets in contact with the various layer surfaces.

Table S3. Contact angle and surface energy of water and formamide on the various electrode systems studied.

Solid surface	Water contact angle	Formamide contact angle	Surface energy [mN/m][a]
PM6	100.4°	82.4°	20.3
PM7-Si	105.8°	83.8°	22.3
BTP-eC9	94.3°	70.8°	29.5
MoO_3	37.7	42.5	59.7
MoO_3/Br-2PACz	62.6	43.0	43.7
ZnO/PFN-Br	71.1	45.7	42.8

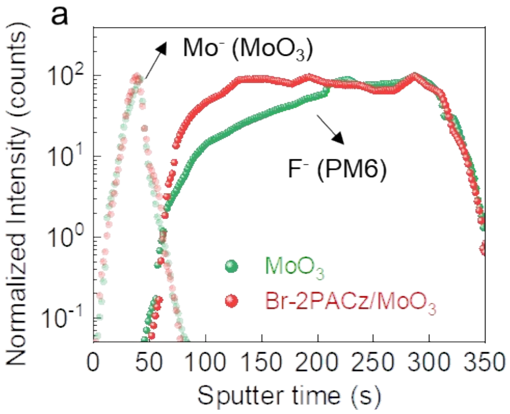

Fig. S6. ToF-SIMS signal intensity as a function of sputtering time for: (a) PM6 and (b) PM7-Si-based cells utilising MoO_3 and Br-2PACz/MoO_3 as the HTLs.

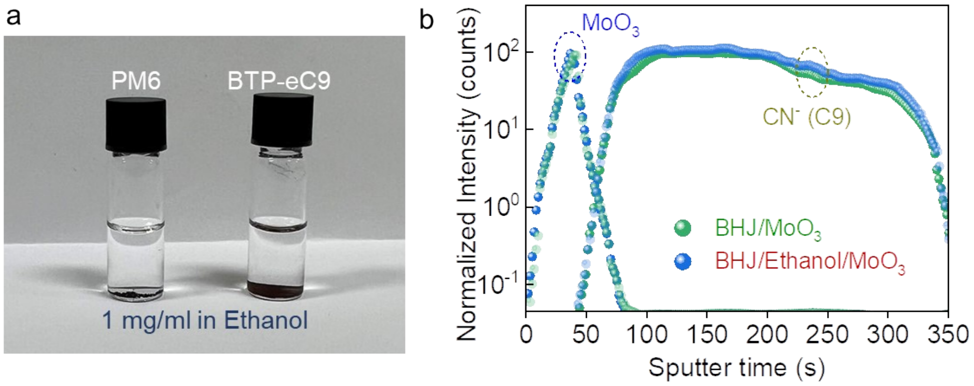

Fig. S7. (a) Picture of PM6 (left) and BTP-eC9 (right) in ethanol with a concentration of 1 mg/ml. Both materials are insoluble in ethanol and precipitate at the bottom of the vials (appear as black solid/powder). (b) ToF-SIMS signal intensity against sputtering time for a cell featuring an as-prepared BHJ/MoO_3 and one where ethanol was spin-coated atop the BHJ before MoO_3 deposition (BHJ/Ethanol/MoO_3).

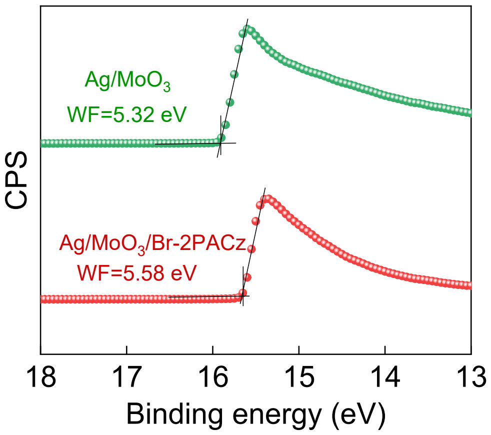

Fig. S8. The UPS results for MoO$_3$ and MoO$_3$/Br-2PACz.

Table S4. Experimentally measured work functions (WF) of MoO$_3$ and MoO$_3$/Br-2PACz using UPS and Kelvin Probe.

Surface	Work function, WF, [eV]	
	via UPS	via KP
MoO$_3$	5.32	5.38
MoO$_3$/Br-2PACz	5.58	5.65
Ag	-	4.3

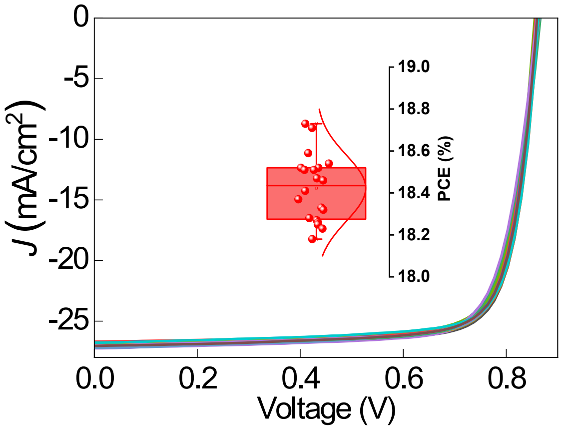

Fig. S9. *J-V* curves of 20 cells based on PM6:PM7-Si:BTP-eC9 with Br-2PACz/MoO$_3$ HEL.

Table S5. The operating parameters of 20 OPV cells based on PM6:PM7-Si:BTP-eC9 with Br-2PACz/MoO$_3$ HEL. The cells were characterised under simulated solar illumination of AM 1.5G (100 mW/cm^2).

Number	V_{OC} [V]	J_{SC} [mA/cm^2]	FF [%]	PCE [%]
1	0.863	27.05	80.3	18.73
2	0.861	26.90	80.8	18.71
3	0.860	27.19	79.5	18.59
4	0.861	26.78	80.4	18.54

5	0.861	26.93	79.9	18.52
6	0.862	26.87	80.0	18.52
7	0.857	26.68	80.9	18.51
8	0.860	27.04	79.6	18.51
9	0.866	27.00	79.0	18.47
10	0.861	26.96	79.5	18.46
11	0.862	26.76	79.8	18.41
12	0.861	26.79	79.8	18.37
13	0.859	26.79	79.7	18.33
14	0.864	27.20	78.0	18.32
15	0.863	27.09	78.3	18.28
16	0.863	27.07	78.3	18.27
17	0.861	26.99	78.7	18.26
18	0.856	26.82	79.3	18.25
19	0.863	26.96	78.2	18.23
20	0.858	26.91	78.7	18.18

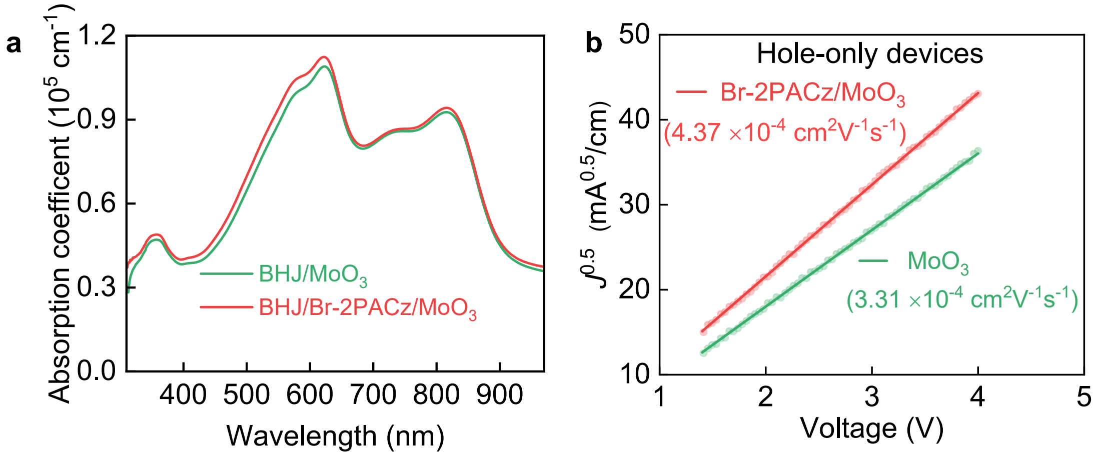

Fig. S10. (a) Absorption coefficient versus wavelength for BHJ/MoO_3 and BHJ/Br-2PACz/MoO_3 films. (b) The SCLC curves of hole-only devices featuring MoO_3 and Br-2PACz/MoO_3 as the HELs.

Table S6. The hole (μ_h) carrier mobility of neat BHJ films with different HELs.

HEL	Thickness of the BHJ [nm]	μ_h [$cm^2\ V^{-1}s^{-1}$]
MoO_3	110	$(3.31\pm0.4)\times10^{-4}$
Br-2PACz/MoO_3	107	$(4.37\pm0.3)\times10^{-4}$

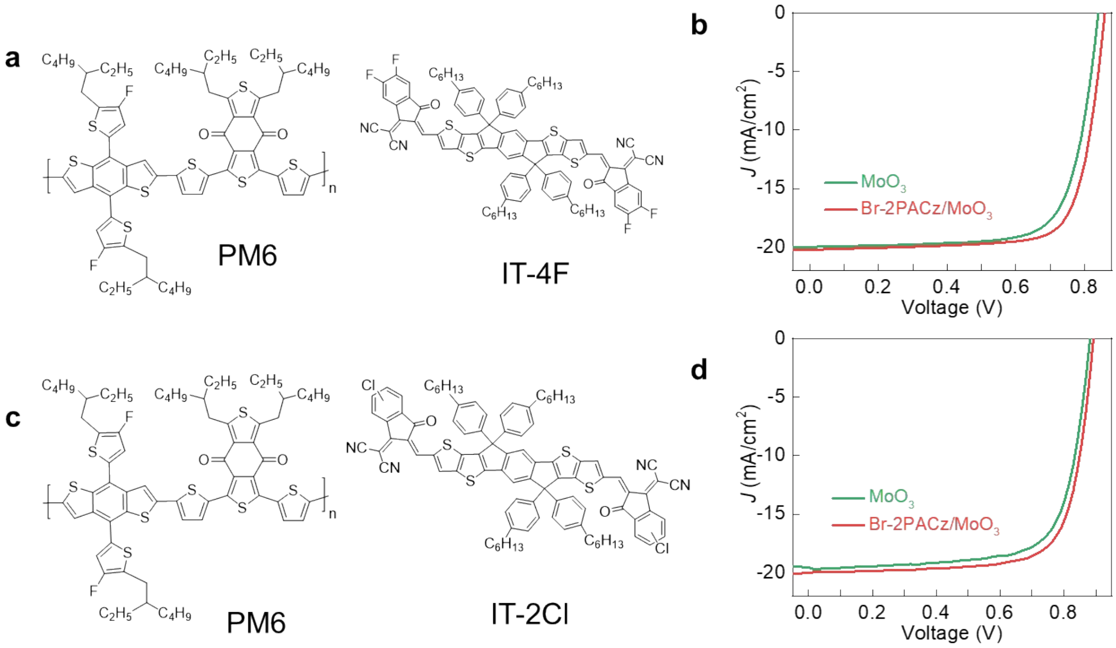

Fig. S11. (a) Chemical structure of PM6 and IT-4F, and (b) *J-V* curves of PM6:IT-4F solar cells based on MoO_3, and Br-2PACz/MoO_3 HELs. (c) Chemical structure of PM6 and IT-2Cl, and (d) *J-V* curves of PM6:IT-2Cl solar cells based on MoO_3, and Br-2PACz/MoO_3 HELs.

Table S7. Summary of key operating parameters of OPVs based on PM6:IT-4F and PM6:IT-2Cl BHJ based on MoO_3, and Br-2PACz/MoO_3 HELs measured under AM 1.5G (100 mW/cm^2).

BHJ	HEL	V_{OC} [V]	J_{sc} [mA/cm^2]	FF [%]	PCE [%]
PM6:IT-4F	MoO_3	0.841	19.97	73.97	12.43 (12.0±0.3)
	Br-2PACz/MoO_3	0.859	20.24	76.17	13.25 (12.7±0.4)
PM6:IT-2Cl	MoO_3	0.881	19.62	74.65	12.81 (12.5±0.2)
	Br-2PACz/MoO_3	0.893	20.01	74.44	13.29 (12.9±0.2)

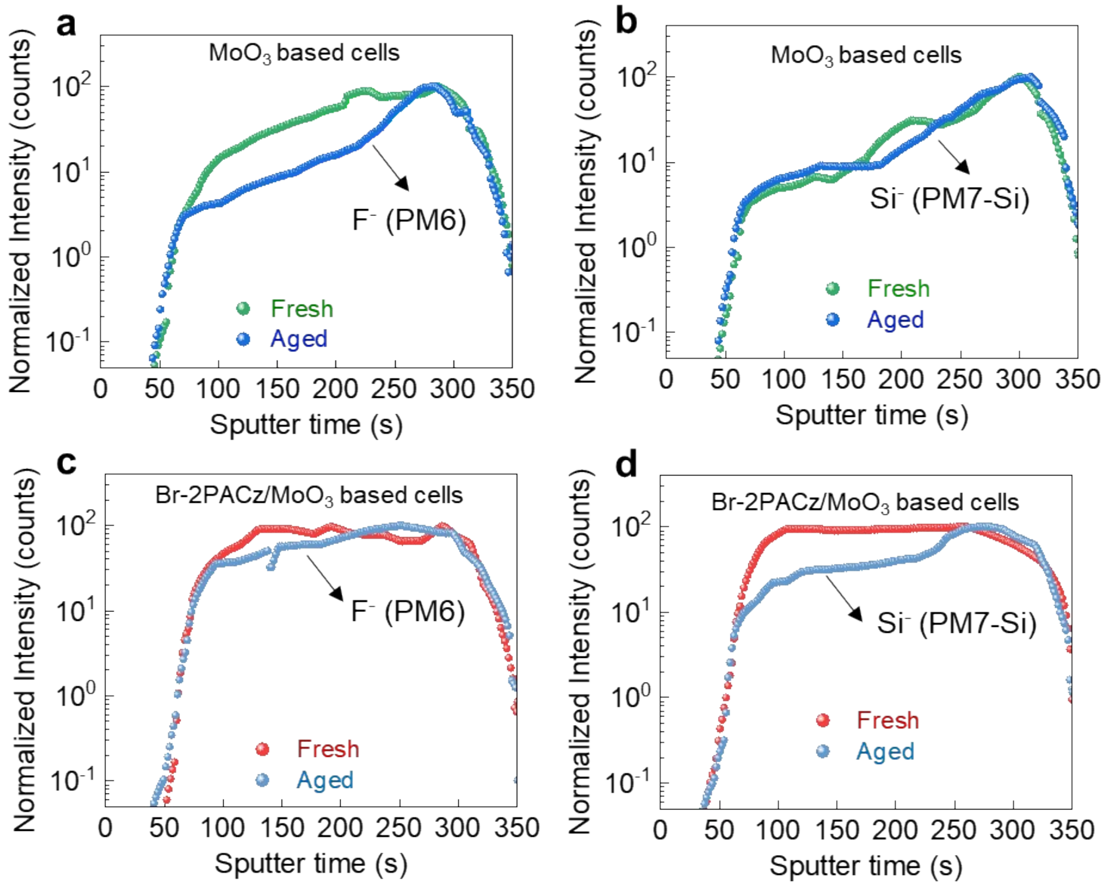

Fig. S12. ToF-SIMS signal versus sputtering time for: (a) PM6 and (b) PM7-Si in MoO_3-based cells, and (c) PM6 and (d) PM7-Si in Br-2PACz/MoO_3-based devices.

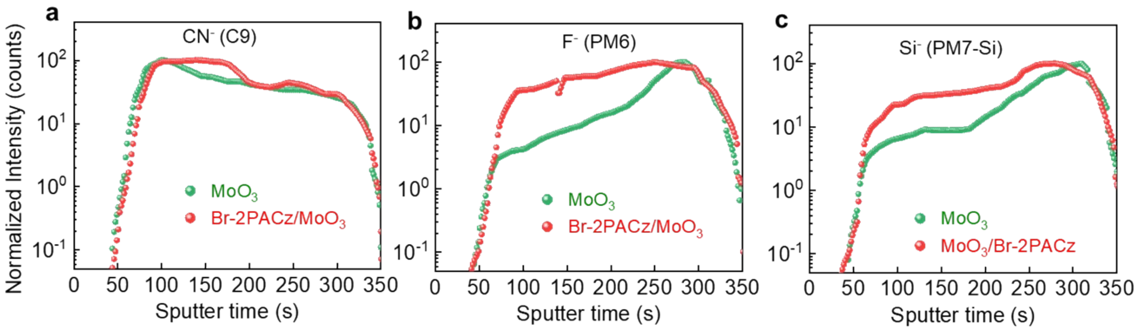

Fig. S13. ToF-SIMS signal versus sputtering time measured for aged PM6:PM7-Si:BTP-eC9 OPVs featuring MoO_3 and Br-2PACz/MoO_3 HTLs. Detected signal associated with the acceptor molecule BTP-eC9 (a), and the donor polymers PM6 (b), and the donor polymer PM7-Si (c).

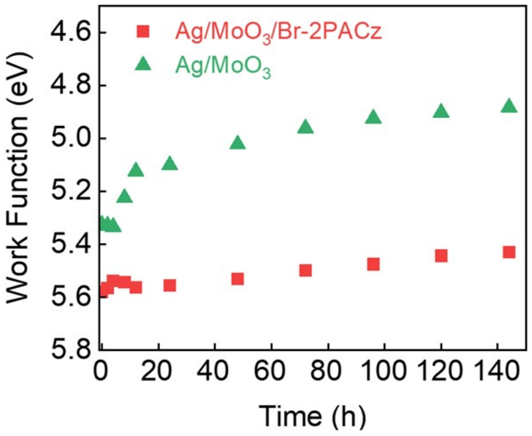

Fig. S14. Evolution of the work functions of Ag/MoO$_3$ and Ag/MoO$_3$/Br-2PACz systems measured via intermittent Kelvin Probe measurements under continuous illumination with white light (100 mW/cm^2) in nitrogen-filled glove box (O$_2$ ≈ 5 ppm and H$_2$O ≈ 0.8 ppm).

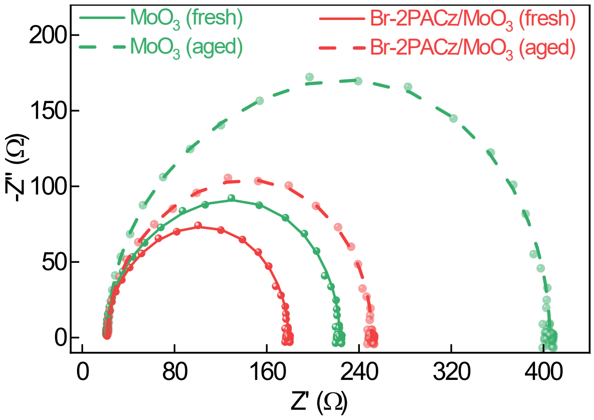

Fig. S15. EIS of fresh and aged OPV cells with MoO$_3$ and Br-2PACz/MoO$_3$.

Table S8. The fitting parameters to the Nyquist plots for the fresh and aged OPVs. R_{ele} corresponds to electrode resistance including ITO and Ag; R_{int} and C_{int} parallel connection corresponds to resistance and capacitance of the interface layer; R_{bhj} and C_{bhj} parallel connection corresponds to resistance and capacitance of the BHJ layer.

Interlayer	Type	R_{ele} [Ω]	R_{inter} [Ω]	C_{inter} [nF]	R_{bhj} [Ω]	C_{bhj} [nF]
MoO$_3$	Fresh	20.5	50.3	18.7	152.5	21.8
	Aged	22.3	103.4	13.7	280.4	2.5
Br-2PACz/MoO$_3$	Fresh	21.3	36.7	35.3	120.8	28.5
	Aged	21.9	55.6	12.8	173.8	13.1

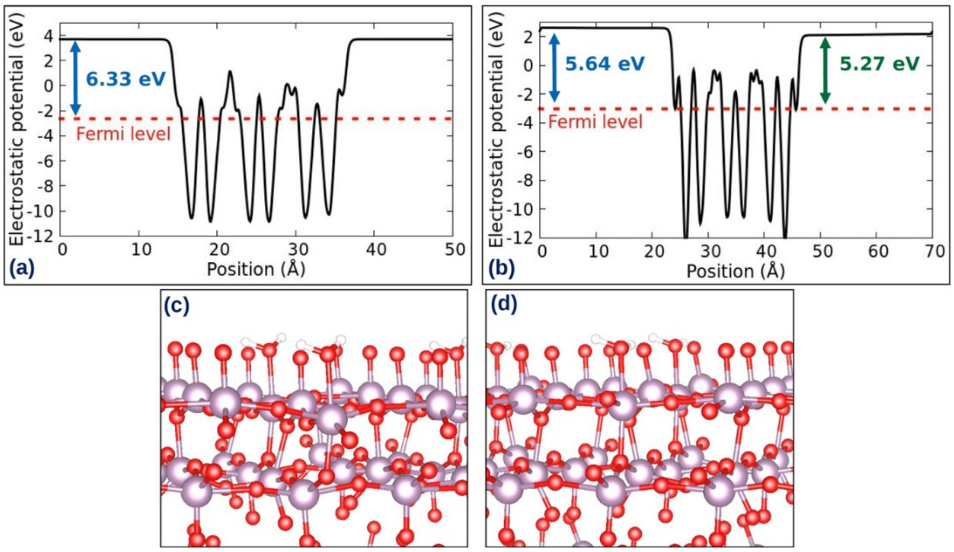

Fig. S16. (a) Plane-averaged electrostatic potential for a $MoO_{2.75}$ slab. The calculated work function (WF) is 6.33 eV. (b) Same as (a), but H_2O molecules are chemisorbed on all surface O vacancies. The WF is 5.27 eV (5.64 eV) for the top (bottom) surface shown in (c) [(d)]. The bottom (top) surface has (does not have) H bonds between the adsorbed H_2O molecules and neighbouring surface O atoms (Mo: light purple, O: red, H: white spheres).

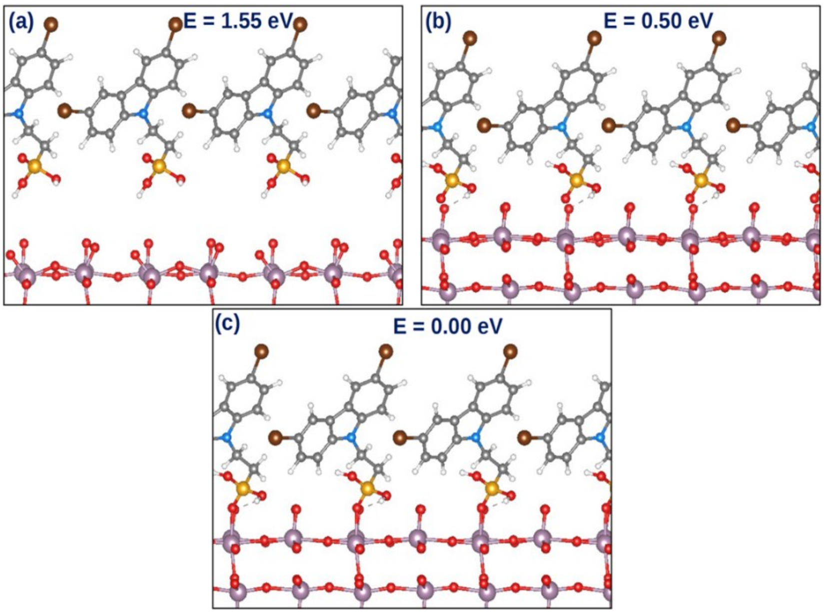

Fig. S17. Br-2PACz adsorption on a $MoO_{2.75}$ surface: (a) Physisorption over surface O atoms, (b) physisorption over O vacancies, (c) chemisorption on O vacancies, Mo-O bonds are formed between the Br-2PACz molecules and Mo atoms (Mo: purple, O: red, C: gray, N: blue, H: white, P: orange, Br: brown spheres). E is the relative energy per Br-2PACz molecule.

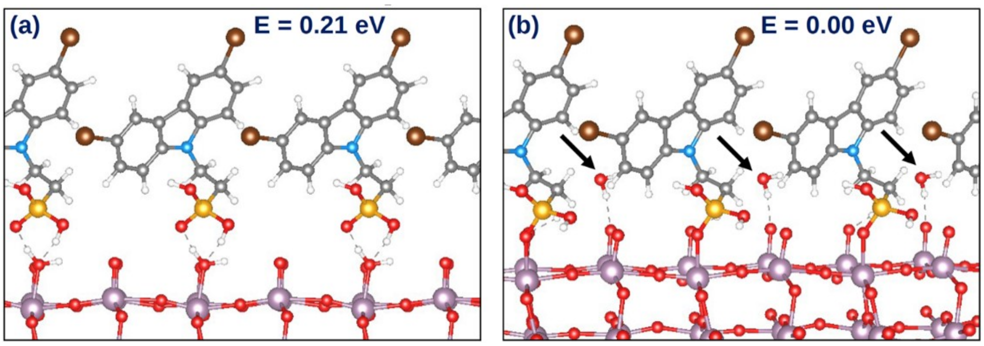

Fig. S18. Br-2PACz adsorption on a H_2O-covered $MoO_{2.75}$ surface: (a) Physisorption over the surface H_2O group, (b) replacement of the H_2O groups by chemisorbed Br-2PACz molecules, the H_2O molecules (shown arrows) remain physisorbed in neighbouring sites (Mo: purple, O: red, C: gray, N: blue, H: white, P: orange, Br: brown spheres). E is the relative energy per Br-2PACz molecule. These results show that Br-2PACz molecules can chemisorb also over H_2O-covered MoO_x surfaces.

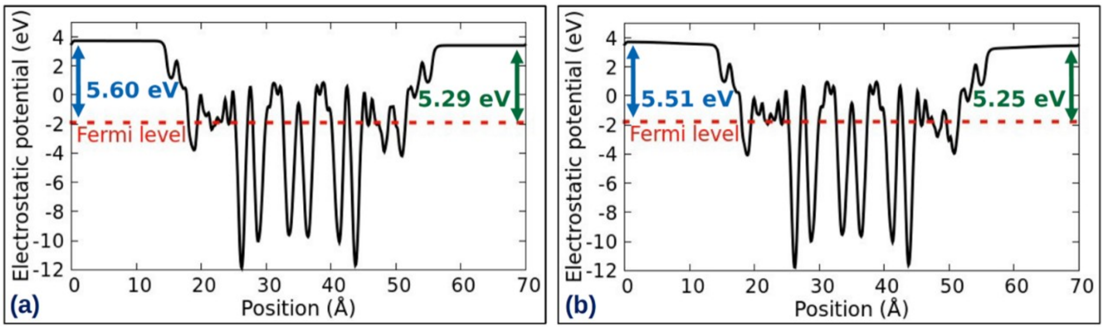

Fig. S19. (a) Plane-averaged electrostatic potential for Br-2PACz on MoO2.75 surfaces. The calculated work function (WF) is 5.29 eV (5.60 eV) for the top (bottom) surface of the slab model. Both surfaces have physisorbed H_2O molecules in configurations similar to that shown in **Fig. S14**, but have small structural differences with respect to their H bonds and relative orientation of the adsorbed molecules. (b) Same for (a), but without physisorbed H_2O molecules.

References

1. W. Peng, Y. Lin, S. Y. Jeong, Y. Firdaus, Z. Genene, A. Nikitaras, L. Tsetseris, H. Y. Woo, W. Zhu, T. D. Anthopoulos and E. Wang, *Chem. Mater*. **2021**, 33, 7254.
2. Y. Lin, Y. Zhang, J. Zhang, M. Marcinskas, T. Malinauskas, A. Magomedov, M. I. Nugraha, D. Kaltsas, D. R. Naphade, G. T. Harrison, A. El-Labban, S.

Barlow, S. De Wolf, E. Wang, I. McCulloch, L. Tsetseris, V. Getautis, S. R. Marder and T. D. Anthopoulos, *Adv. Energy Mater.*, 2022, 2202503..

3. G. Kresse and J. Furthmüller, *Phys. Rev. B*, 1996, **54**, 11169.
4. P. E. Blochl, *Phys. Rev. B*, 1994, **50**, 17953-17979.
5. J. P. Perdew, K. Burke and M. Ernzerhof, *Phys. Rev. Lett.*, 1996, **77**, 3865.
6. K. Momma and F. Izumi, *J. Appl. Crystallogr.*, 2011, **44**, 1272-1276.
7. V. Wang, N. Xu, J.-C. Liu, G. Tang and W.-T. Geng, *Comput. Phys. Commun.*, 2021, **267**, 108033.
8. C. Li, J. Zhou, J. Song, J. Xu, H. Zhang, X. Zhang, J. Guo, L. Zhu, D. Wei, G. Han, J. Min, Y. Zhang, Z. Xie, Y. Yi, H. Yan, F. Gao, F. Liu and Y. Sun, *Nat. Energy*, 2021, **6**, 605-613.
9. J. Huang, D. Zhao, Z. Dou, Q. Fan, N. Li, S. Peng, H. Liu, Y. Jiang, J. Yu and C.-Z. Li, *Energ. Environ. Sci.*, 2021, **14**, 3010-3018.
10. Z. Abbas, S. U. Ryu, M. Haris, C. E. Song, H. K. Lee, S. K. Lee, W. S. Shin, T. Park and J.-C. Lee, *Nano Energy*, 2022, **101**, 107574.
11. X. Song, G. Liu, W. Gao, Y. Di, Y. Yang, F. Li, S. Zhou and J. Zhang, *Small*, 2021, **17**, 2006387.
12. Y. B. Lin, Y. Firdaus, M. I. Nugraha, F. Liu, S. Karuthedath, A. H. Emwas, W. M. Zhang, A. Seitkhan, M. Neophytou, H. Faber, E. Yengel, I. McCulloch, L. Tsetseris, F. Laquai and T. D. Anthopoulos, *Adv. Sci.*, 2020, **7**, 1903419.
13. C. Zhu, J. Yuan, F. Cai, L. Meng, H. Zhang, H. Chen, J. Li, B. Qiu, H. Peng, S. Chen, Y. Hu, C. Yang, F. Gao, Y. Zou and Y. Li, *Energ. Environ. Sci*, 2020, **13**, 2459-2466.
14. Y. Cui, H. Yao, J. Zhang, T. Zhang, Y. Wang, L. Hong, K. Xian, B. Xu, S. Zhang, J. Peng, Z. Wei, F. Gao and J. Hou, *Nat. Commun.*, 2019, **10**, 2515.
15. C. Sun, S. Qin, R. Wang, S. Chen, F. Pan, B. Qiu, Z. Shang, L. Meng, C. Zhang, M. Xiao, C. Yang and Y. Li, *J. Am. Chem.. Soc*, 2020, **142**, 1465-1474.
16. H. Wang, T. Liu, J. Zhou, D. Mo, L. Han, H. Lai, H. Chen, N. Zheng, Y. Zhu, Z. Xie and F. He, *Adv. Sci.*, 2020, **7**, 1903784.
17. Y. Jiang, X. Dong, L. Sun, T. Liu, F. Qin, C. Xie, P. Jiang, L. Hu, X. Lu, X. Zhou, W. Meng, N. Li, C. J. Brabec and Y. Zhou, *Nat. Energy*, 2022, **7**, 352-359.
18. Y. Yang, J. Wang, P. Bi, Q. Kang, Z. Zheng, B. Xu and J. Hou, *Adv. Sci.*, 2022, **34**, 6312-6322.
19. L. Zhu, M. Zhang, J. Xu, C. Li, J. Yan, G. Zhou, W. Zhong, T. Hao, J. Song and X. Xue, *Nat. Mater.*, 2022, **21**, 656-663.
20. R. Sun, Y. Wu, X. Yang, Y. Gao, Z. Chen, K. Li, J. Qiao, T. Wang, J. Guo, C. Liu, X. Hao, H. Zhu and J. Min, *Adv. Mater.* 2022, 2110147.
21. Y. Wei, Z. Chen, G. Lu, N. Yu, C. Li, J. Gao, X. Gu, X. Hao, G. Lu, Z. Tang, J. Zhang, Z. Wei, X. Zhang and H. Huang, *Adv. Mater.* 2022, 2204718.
22. K. Chong, X. Xu, H. Meng, J. Xue, L. Yu, W. Ma and Q. Peng, *Adv. Mater.*, 2022, **34**, 2109516.
23. W. Gao, F. Qi, Z. Peng, F. R. Lin, K. Jiang, C. Zhong, W. Kaminsky, Z. Guan, C. S. Lee, T. J. Marks, H. Ade and A. K. Jen, *Adv. Mater*, 2022, 2202089.

24. P. Bi, S. Zhang, Z. Chen, Y. Xu, Y. Cui, T. Zhang, J. Ren, J. Qin, L. Hong, X. Hao and J. Hou, *Joule*, 2021, **5**, 2408-2419.
25. L. Zhan, S. Li, Y. Li, R. Sun, J. Min, Z. Bi, W. Ma, Z. Chen, G. Zhou, H. Zhu, M. Shi, L. Zuo and H. Chen, *Joule*, 2022, **6**, 662-675.
26. Y. Cai, Y. Li, R. Wang, H. Wu, Z. Chen, J. Zhang, Z. Ma, X. Hao, Y. Zhao, C. Zhang, F. Huang and Y. Sun, *Adv. Mater.*, 2021, **33**, 2101733.
27. T. Zhang, C. An, P. Bi, Q. Lv, J. Qin, L. Hong, Y. Cui, S. Zhang and J. Hou, *Adv. Energy Mater.*, 2021, **11**, 2101705.
28. Y. Lin, A. Magomedov, Y. Firdaus, D. Kaltsas, A. El-Labban, H. Faber, D. R. Naphade, E. Yengel, X. Zheng, E. Yarali, N. Chaturvedi, K. Loganathan, D. Gkeka, S. H. AlShammari, O. M. Bakr, F. Laquai, L. Tsetseris, V. Getautis and T. D. Anthopoulos, *ChemSusChem*, 2021, **14**, 3569-3578.
29. W. Peng, Y. Lin, S. Y. Jeong, Z. Genene, A. Magomedov, H. Y. Woo, C. Chen, W. Wahyudi, Q. Tao, J. Deng, Y. Han, V. Getautis, W. Zhu, T. D. Anthopoulos and E. Wang, *Nano Energy*, 2022, **92**, 106681.